Available online at www.sciencedirect.com
SCIENCE DIRECT®
Journal of Solid State Chemistry 172 (2003) 73–80
JOURNAL OF SOLID STATE CHEMISTRY
http://elsevier.com/locate/jssc

Substitution of Co^{3+} in $YBa_2Fe_3O_8$

Q.Z. Huang,[a] Vicky Lynn Karen,[b] A. Santoro,[a] A. Kjekshus,[c] J. Lindén,[d] T. Pietari,[e] and P. Karen[c,*]

[a] *NIST Center for Neutron Research, Gaithersburg, MD 20899, USA*
[b] *Ceramics Division, NIST, Gaithersburg, MD 20899, USA*
[c] *Department of Chemistry, University of Oslo, Blindern, N-0315 Oslo, Norway*
[d] *Department of Physics, Åbo Akademi, FI-20500 Turku, Finland*
[e] *Department of Technical Physics, Helsinki University of Technology, FI-02150 Espoo, Finland*

Received 27 June 2002; received in revised form 3 October 2002; accepted 7 October 2002

Abstract

The accommodation of Co in the oxygen-saturated solid-solution phase $YBa_2(Fe_{1-z}Co_z)_3O_{8+w}$ has been investigated by powder X-ray and neutron diffraction techniques, as well as by ^{57}Fe Mössbauer spectroscopy. Of the nominal composition range $0.00 \leqslant z \leqslant 1.00$ tested, the solid-solution limit under syntheses at 950°C in 1 bar O_2 is $z = 0.47(5)$. No symmetry change in the nuclear and magnetic structures is seen as a consequence of the Co substitution, and the Co atoms are distributed evenly over the two sites that are square-pyramidally and octahedrally coordinated for $w = 0$. The oxygen-saturated samples maintain their oxygen content roughly constant throughout the homogeneity range, showing that Co^{3+} replaces Fe^{3+}. Despite the nearly constant value of w, Mössbauer spectroscopy shows that the amount of tetravalent Fe slightly increases with increasing z, and this allows Co to adopt valence close to 3.00 to a good approximation. The magnitude of the antiferromagnetic moment (located in the a, b plane) decreases with z in accordance with the high-spin states of the majority Fe^{3+} and Co^{3+} ions. Bond-valence analyses are performed to illustrate how the structural network becomes increasingly frustrated as a result of the substitution of Fe^{3+} by the smaller Co^{3+} ion. A contrast is pointed out with the substitution of cobalt in $YBa_2Cu_3O_7$ where it is a larger Co^{2+} ion that replaces smaller Cu^{2+}.

Keywords: Yttrium-barium-iron-cobalt oxide; Solid-solution phase; Triple-perovskite-type structure; Antiferromagnetism; ^{57}Fe Mössbauer spectra

1. Introduction

The structure of the ordered perovskite variant $AA'_2T_3O_{9-\delta}$ with triplicate unit cell and two types of transition metal (T) coordinations is an excellent charge buffer, where redox processes take place predominantly in one of the T coordination spheres. In $YBa_2Cu_3O_{6+w'}$, this arrangement causes superconductivity to occur over most of the homogeneity range [1,2], and maintains high electronic and ionic conductivity at higher temperatures. The latter feature can be utilized in applications like ceramic semi-permeable membranes, oxygen pumps, oxide fuel-cell cathodes, and sensors. However, since Cu is a noble metal, cuprates are not particularly redox stable. The $YBa_2Fe_3O_8$ phase [3] is the hitherto only example of an analogue of $YBa_2Cu_3O_7$ where Cu is fully replaced by another transition metal, while the Y and Ba sites are left intact. The oxygen content variations in $YBa_2Fe_3O_{8+w}$ are limited to some $-0.25 < w < 0.10$ [4,5].

A complete replacement of Cu in the $YBa_2Cu_3O_7$-type structure by first-row transition metals or Au has been tested by the present authors under conditions (temperature, partial pressure of oxygen) appropriate to the presumed stabilization of di- or trivalent ions of these metals. With the notable exception of Fe, all attempted substitutions yielded a disordered perovskite or mixtures of phases which are thus more stable than the triple-perovskite arrangement. For example, Sc forms a disordered perovskite, Ti (at very low p_{O_2}'s) forms a (light-blue colored) mixture of the $(Y_{0.2}Ba_{0.8})TiO_3$ perovskite and the $Y_2Ti_2O_7$ pyrochlore, and Au gives an ordered Ba_2AuYO_6 perovskite phase together with unreacted Au.

*Corresponding author. Fax: +22-85-54-41.
E-mail address: pavel.karen@kjemi.uio.no (P. Karen).

0022-4596/03/$ - see front matter © 2002 Elsevier Science (USA). All rights reserved.
doi:10.1016/S0022-4596(02)00122-6

Cobalt, of all transition metals, is the most compatible with the $YBa_2Cu_3O_7$-type structure, judged from the fact that Co is able to substitute for about $\frac{1}{3}$ of the Cu atoms in the prototype [6]. Considering its resemblance to Fe, it is interesting to see how Co is accommodated in the $YBa_2Fe_3O_8$ structure. The answer is not obvious, given the remarkable fact that $YBa_2Fe_3O_8$ can host only a rather limited amount of Cu (up to $z = 0.07$) at the Fe sites [7]. Since these differences are clearly rooted in structure–chemical features, we synthesized a $YBa_2(Fe_{1-z}Co_z)_3O_{8+w}$ series with well-defined oxygen content, and used powder X-ray and neutron diffraction as well as ^{57}Fe Mössbauer spectroscopy to examine the structural and magnetic properties of these solid solutions.

2. Experimental

2.1. Synthesis

Samples were prepared by firing of precursor materials obtained from liquid-mixed citrates [8]. Standardized reagent grade components were used. Annealed yttrium oxide (99.99%, Megon) was dissolved in boiling citric acid monohydrate (Fluka), the solution was cooled down, an equal amount of water was added and barium carbonate (0.8% Sr, Merck) was dissolved. The iron and cobalt components were added as a formate solution, prepared from Fe (powder, 99.9 + %, Aldrich Chemicals) and Co (sponge, 99.9%, Johnson–Matthey), by dissolution in a hot, 50% aqueous solution of formic acid. The mixed citrate solution was evaporated into a viscous melt, which was dehydrated at 180°C into a brown solid, milled and incinerated in air at 450°C. The precursor was pressed into pellets and fired four times for 100 h in an atmosphere of flowing O_2, with intermittent rehomogenizations. Owing to the low solidus in certain parts of the phase diagram, the firing temperature was gradually increased from 900°C to 950°C. The firing was followed by free cooling in the furnace over several hours. The bulk samples from the solid-solution range were subsequently oxidized in a 1 bar O_2 atmosphere at 400°C for 100 h.

2.2. Oxygen content control

A second series of (small-scale) samples was sintered from selected bulk solid-solution samples ($z = 0.2, 0.4, 0.5$) at 1040°C in oxygen and used to test the solid-state redox behavior at 950°C (the bulk synthesis temperature). These samples were equilibrated for several days in wet mixtures of oxygen and argon (p_{H_2O} defined by saturated solution of KBr) and quenched into a metallic container filled with dried argon gas of high purity. A thin surface layer was ground off the samples before they were analyzed.

2.3. Powder X-ray diffraction (PXD)

The phase purity and unit-cell parameters were evaluated with the help of the SCANPI package of programs [9] from PXD data obtained using a Guinier–Hägg camera with Cu$K\alpha_1$ radiation and Si as an internal standard. Quantitative estimates of the phase content were done based on comparisons of observed and calculated intensities [10], using up to three (low-angle) Bragg reflections.

2.4. Powder neutron diffraction (PND)

Unpolarized PND measurements were made at 295 K at the Reactor of the National Institute of Standards and Technology, using the experimental conditions specified in Table 1. All refinements were carried out using the Rietveld method [11] adapted to the multicounter diffractometer arrangements using the GSAS program of Larson and Von Dreele [12].

2.5. Oxygen content analyses

The overall oxygen content in the (second series) small-scale samples was determined by cerimetric analysis via reverse titration of Mohr's salt, $(NH_4)_2Fe(SO_4)_2 \cdot 6H_2O$, which was standardized in a crystalline form of a certain particle size (0.1–0.5 mm) by sieving. Finely powdered samples, with up to twice their weight of the Mohr's salt added, were warm-digested in concentrated hydrochloric acid (with a water overlayer) in glass ampoules sealed under argon. Ultrasound was used to disperse the powders under the dissolution process. Titrations were performed in argon-filled titration flasks, with ferroin as an indicator, in solutions containing concentrated H_3PO_4 in amounts sufficient to decompose most of the green $CoCl_4^{2-}$ ions. Concentrated HCl was used to control pH in order to prevent hydrolysis of the titration solution

Table 1
Collection of PND-intensity data

Monochromatic beam	311 reflection from a Cu crystal
Wavelength (Å)	1.5396
Horizontal divergences	15′, 20′, 7′ of arc for the in-pile, monochromatic beam, and diffracted beam collimators, respectively
Sample containers	Vanadium cans
2Θ angular range	3–168°, steps: 0.05°
Scattering amplitudes (fm)	b(Y) = 775, b(Ba) = 525, b(Fe) = 954, b(Co) = 253, b(O) = 581

into transparent drops on the walls of the titration flasks. This was necessary in particular for samples with high Co content where increasing amounts of the Mohr's salt were required, having the undesirable side effect of a pH-buffer. The standard error of such titrations increases, and for determination of the oxygen contents in the (first-series) bulk samples, Rietveld refinements of the PND data were relied upon.

2.6. Mössbauer spectroscopy

Mössbauer spectra were recorded at room temperature in transmission geometry and fitted using the full Hamiltonian of combined electric and magnetic interactions. The Mössbauer absorbers were prepared by mixing ~80 mg of sample material with varnish and evenly distributing it on an aluminum foil. The absorber diameter was ~19 mm. The measurements were performed in Dec. 1998 with an Amersham $^{57}Co:Rh$ (20 mCi, January 1995) source. A linear velocity scale with a maximum of 15 mm/s was applied. The following principal hyperfine parameters were obtained from the fitted spectra: the internal magnetic field experienced by the Fe nucleus (B), the chemical isomer shift relative to α-Fe (δ), the quadrupole coupling constant (eQV_{zz}), the resonance line width (Γ), and the relative intensities of the components (I). The following conditions and constraints were applied: (i) Each component was allowed a certain variation in the parameter B, in order to simulate the effect of local distortions of the coordination polyhedra (see Ref. [13]). A Gaussian distribution was assumed and its width (ΔB) was introduced as a fit parameter. Components corresponding to various valence states were allowed to have different values of ΔB. The resonance line width (Γ) was the same for all components. In the actual fits, the maximum values for ΔB were found to vary between 2.0 and 2.8 T for the most intense Fe(1)-site component and between 0.8 and 1.0 T for the Fe(2)-site component. (ii) According to Ref. [14], the internal magnetic field in $YBa_2Fe_3O_{8+w}$ is perpendicular to the c-axis, while the main component V_{zz} of the electric field gradient (EFG) lies along c for both the five- and six-coordinated Fe(2) and Fe(1) sites. In the fitting procedure, the angle θ between V_{zz} and B was thus given an initial value of 90°. The asymmetry parameter η of EFG was set to zero in order to keep the number of refined parameters low. That this constraint is actually true for the major components for the tetragonal phase was also tested in practice. (iii) A small asymmetric quadrupole component, originating from traces of iron in the Be detector window and in the Al was kept fixed during the fit. The latter impurity defect covers less than 2% of the spectral intensity obtained in the measurements.

3. Results

3.1. Synthesis and characterization

3.1.1. Oxygen-saturated samples

Synthesis of a nominal oxygen-saturated substitution series was attempted for $z_{nom} = 0, 0.2, 0.3, 0.4, 0.5, 0.6, 0.8$ and 1. The presence of the triple-perovskite-type solid-solution phase $YBa_2(Fe_{1-z}Co_z)_3O_{8+w}$ is observed up to $z_{nom} = 0.8$, but above $z_{nom} = 0.5$ the multiphase abundance increases. For $z_{nom} = 0.2, 0.3, 0.4$ and 0.5, a small amount (~2 wt%) of a cubic perovskite occurs. According to the estimated unit-cell parameters of ~4.10 Å, this phase represents a (Co-poor) disordered solid solution (Ba,Y)(Co,Fe,Y)$O_{\sim 3}$. Its location in close vicinity of the desired phase in the phase diagram [4] makes it easy to occur as a consequence of minor deviations in the composition of the starting materials or various intersite equilibria. At $z_{nom} = 0.6$, the amount of this cubic perovskite phase [$a = 4.1197(11)$ Å] has increased to 6 wt% and for $z_{nom} = 0.8$ it represents about 50 wt% of the product [$a = 4.0848(3)$ Å]. The rest of the $z_{nom} = 0.8$ sample is composed of approximately equal portions of the triple-perovskite-type oxide and a hexagonal $BaCoO_{3-w''}$-type phase, accompanied by some 5 wt% of an unidentified, apparently Co-rich oxide. The sample with $z_{nom} = 1$ contains neither the triple- nor single-perovskite-type phase and consists of $BaCoO_{3-w''}$ (~70 wt%), Y_2O_3 (~20 wt%) and an unidentified oxide (~10 wt%, different from the $z = 0.8$ sample). The $BaCoO_{3-w''}$ oxide occurs in its 12H stacking-sequence variant [15], with $w'' \approx 0.4$ [$a = 5.6712(8)$ Å, $c = 28.429(13)$ Å] clearly manifested in the PXD pattern, inter alia, by the Bragg line at $d = 14.25$ Å. This accords also well with the conditions during firing (950°C, 1 bar O_2) when related to the phase diagram by Negas and Roth [16]. The stacking-sequence ordering of $BaCoO_{3-w''}$ depends strongly on w'', and the PXD pattern of the nominal $z_{nom} = 1$ samples hence changes profoundly as a function of the synthesis temperature.

From the composition of the multiphase samples, the solid-solubility limit for $YBa_2(Fe_{1-z}Co_z)_3O_{8+w}$ is estimated to be around $z = 0.50$. Another estimate is obtained from the unit-cell volume as a function of the nominal composition parameter z_{nom}. The plot is shown in Fig. 1, giving $z = 0.47(5)$ as the limit by least-squares fitting. Having distinct Bragg 001 and 112 lines in their PXD patterns, the samples were clearly of the triple-perovskite-type, but the lattice metrics were pseudocubic ($c = 3a$) on the resolution scale of the Guinier–Hägg camera. Since this prevents extraction of lattice parameters with meaningful precision, unit-cell volumes were evaluated instead, viz., from Si-standardized PXD data; for PND data see Table 2.

3.1.2. Solid solutions with varied oxygen content

Equilibrium oxygen contents of the $YBa_2(Fe_{1-z}Co_z)_3O_{8+w}$ samples ($z = 0.2$, 0.4 and 0.5) at several relatively high partial pressures of oxygen for 950°C are listed in Table 3. The data show that the average Fe/Co valences at the synthesis temperature are close to +3 ($w = 0$) and decrease as a function of decreasing p_{O_2}. As a function of z, the equilibrium oxygen contents diminish increasingly. As an example, the difference in the oxygen content between $z = 0.5$ and 0.4 is always larger than that between $z = 0.4$ and 0.2. This suggests that iron under given conditions is somewhat closer than cobalt to the intrinsic trivalent state where valences vary least as a function of the partial pressure of oxygen. Since the equilibrium oxygen contents for $p_{O_2} = 1$ bar (Table 3) remain well above $w \approx -0.25$ that marks the lower stability limit for the parent phase with respect to the oxygen content [17], a redox instability under synthesis conditions is not a key factor in defining the solid-solubility limit for Co in $YBa_2(Fe_{1-z}Co_z)_3O_{8+w}$.

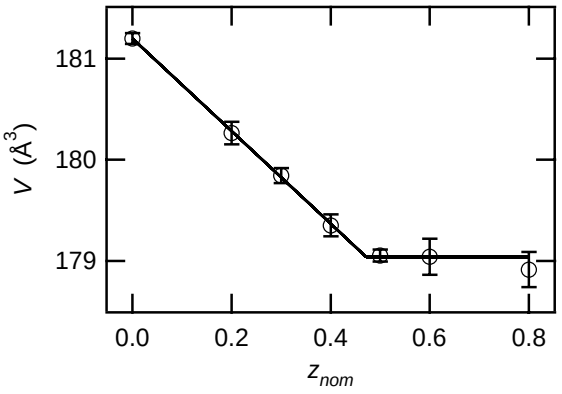

Fig. 1. PXD unit-cell volume of the triple-perovskite-type $YBa_2(Fe_{1-z}Co_z)_3O_{8+w}$ phase as a function of the nominal composition parameter z_{nom}. Lines according to weighted least-squares fits.

3.2. Neutron diffraction

The structure refinements of the PND data were carried out in space group $P4/mmm$ using as input parameters those obtained in the previous analyses for $YBa_2Fe_3O_{8+w}$ [3,18]. In particular, the refinements assumed the same split-site model for the effect of the additional oxygen atoms w on its neighbors as described in Ref. [18], with the temperature factor of O(4) fixed at a reasonable value in order to avoid correlation with the occupancy. The magnetic PND intensities for

Table 2
Refined structural parameters for $YBa_2(Fe_{1-z}Co_z)_3O_{8+w}$ at 295 K

Atom	Parameter	$z = 0.0$	$z = 0.2$	$z = 0.3$	$z = 0.4$	$z = 0.5$
	a (Å)	3.9152(1)	3.9122(1)	3.9087	3.9061(1)	3.9049(1)
	c (Å)	11.8106(4)	11.7704(4)	11.7555(4)	11.7279(4)	11.7168(4)
	V (Å^3)	181.04(2)	180.15(2)	179.60(2)	179.24(2)	178.82(2)
Y	B (Å^2)	0.75(4)	0.44(4)	0.49(5)	0.62(4)	0.60(4)
Ba	z	0.1662(3)	0.1669(3)	0.1681(3)	0.1657(3)	0.1688(3)
	B (Å^2)	0.71(4)	0.69(4)	0.70(5)	0.64(4)	0.67(4)
Fe/Co(1)	B (Å^2)	0.40(4)	0.29(4)	0.20(5)	0.28(6)	0.27(5)
	n	1/0	0.80(1)/0.20(1)	0.69(1)/0.31(1)	0.59(1)/0.41(1)	0.50(1)/0.50(1)
	μ_{AF} (μ_B)	3.41(2)	3.37(2)	3.24(2)	3.28(2)	3.09(2)
Fe/Co(2)	z	0.3396(2)	0.3397(2)	0.3396(2)	0.3389(2)	0.3391(2)
	B (Å^2)	0.49(2)	0.53(3)	0.49(3)	0.58(3)	0.52(3)
	n	1/0	0.80(1)/0.20(1)	0.70(1)/0.30(1)	0.60(1)/0.40(1)	0.50(1)/0.50(1)
	μ_{AF} (μ_B)	3.41(2)	3.37(2)	3.24(2)	3.28(2)	3.09(2)
O(1)	z	0.1824(3)	0.1827(3)	0.1822(3)	0.1833(3)	0.1828(3)
	B (Å^2)	0.95(4)	0.91(4)	1.02(5)	0.91(4)	1.12(5)
O(2)	z	0.3820(2)	0.3816(2)	0.3813(2)	0.3817(2)	0.3815(2)
	B (Å^2)	0.56(4)	0.53(4)	0.56(4)	0.63(3)	0.63(4)
	n	0.932(5)	0.966(5)	0.967(6)	0.974(4)	0.953(4)
O(2′)	z	0.3396(1)	0.3397(1)	0.3396(1)	0.3389(2)	0.3391(2)
	B (Å^2)	0.56(4)	0.53(4)	0.56(4)	0.63(3)	0.63(4)
	n	0.068(5)	0.034(5)	0.033(6)	0.026(4)	0.047(4)
O(3)	B (Å^2)	0.66(4)	0.68(4)	0.79(5)	0.90(4)	0.87(4)
O(4)	B (Å^2)	0.8	0.8	0.8	0.8	0.8
	$n \equiv w$	0.068(5)	0.034(5)	0.033(6)	0.026(4)	0.047(4)
	R_p (%)	5.96	6.29	6.26	5.83	6.00
	R_{wp} (%)	7.65	7.96	7.90	7.37	7.63
	χ^2	1.255	1.541	1.856	2.108	1.617

Space group $P4/mmm$: Y$[\frac{1}{2},\frac{1}{2},\frac{1}{2}]$, Ba$[\frac{1}{2},\frac{1}{2},z]$, Fe/Co(1)$[0,0,0]$, Fe/Co(2)$[0,0,z]$, O(1)$[0,0,z]$, O(2)$[\frac{1}{2},0,z]$, O(2′)$[\frac{1}{2},0,z]$, O(3)$[\frac{1}{2},0,0]$, O(4)$[0,0,\frac{1}{2}]$. Constraints: z for Fe/Co(2) and O(2′) were constrained equal. B of O(4) fixed to an estimate.

$YBa_2(Fe_{1-z}Co_z)_3O_{8+w}$ could be accounted for by the antiferromagnetic (AF) model reported [3,18] for unsubstituted $YBa_2Fe_3O_{8+w}$. The final results (Table 2; with figures of merit matching those reported in Refs. [3,18]) were obtained in every case from refinements in which the atomic, magnetic, and profile parameters were varied simultaneously. A decrease in the ordered magnetic moment μ_{AF} (note, values obtained at 295 K) is seen as a function of the Co substitution level z. Considering, in a reasonable approximation, trivalent states for both Fe and Co, the *decrease* corresponds very well to the replacement of the d^5, $S = \frac{5}{2}$, high-spin (HS) state of iron with the d^6, $S = 2$, HS state of cobalt, predicting the spin-only moment for $z = 0.5$ to be 3.07 μ_B given the refined moment of 3.41 μ_B at $z = 0$ (see Table 2). The antiparallel arranged magnetic moments are located within the a, b plane, but their exact directions could not be resolved.

The PND refinements show that Fe and Co atoms are randomly distributed over the two structural sites which for $w = 0$ would have octahedral and square pyramidal coordinations. The refined content of the excess oxygens ($nO(4) = w$, see Table 2) changes very little as a function of z and, most importantly, it is maintained as $w > 0$ throughout the entire solid-solution range (for these oxygen-saturated samples). In other words, the average oxidation state of Co and Fe is nearly constant. As dictated by the contraction of the unit cell originating from to the somewhat smaller size of HS Co^{3+} than HS Fe^{3+}, interatomic distances in Table 4 generally shorten. The shortening is nearly uniform for all bonds, and this further confirms a homogeneous random replacement during the substitution.

A more detailed insight into the structural consequences of the Co substitution for Fe can be obtained from bond-valence analyses. Table 5 lists bond-valence sums for each crystallographically different atom, calculated using the single-bond lengths (metal–oxygen, in Å) according to Brown [19]: Y 2.019, Ba 2.285, Fe^{2+} 1.734, Fe^{3+} 1.759, Fe^{4+} 1.78 and Co^{3+} 1.700, the actual one for iron (which depends significantly on the valence) being derived iteratively from the resulting bond-valence sum at individual coordinations. It is most instructive to look first at the parent structure ($z = 0.0$). Clearly, the main problem of this triple-perovskite-type phase is that barium is heavily overbonded (bonds too short) and yttrium underbonded while the Fe/Co(1) and Fe/Co(2) sites with different coordination numbers struggle to fulfill the Pauling's rule of parsimony and maintain equal valence (as well as equal magnetic moment in the ordered AF structure). The presence of Co makes things worse owing to its smaller single-bond radius than Fe. Both octahedral and square pyramidal sites then become underbonded, while the overbonding at Ba cannot and does not increase much more. In this situation, the added oxygens O(4) are most welcome to compensate for the bond-valence loss in the square-pyramidal coordinations of Fe/Co(2), and this perhaps explains

Table 3
Cerimetric oxygen contents and PXD unit-cell volumes for $YBa_2(Fe_{1-z}Co_z)_3O_{8+w}$ quenched from 950°C at various partial pressures of oxygen

z	p_{O_2} (bar)	$8 + w$	V (Å^3)
0.0	0.99	8.072(4)	181.19(5)
0.2	0.99	8.042(1)	180.23(12)
0.4	0.99	7.994(1)	179.41(18)
0.5	0.99	7.930(1)	179.23(20)
0.2	0.099	8.004(1)	180.37(11)
0.4	0.099	7.984(13)	179.38(8)
0.5	0.099	7.870(30)	179.34(14)
0.2	0.0053	7.967(5)	180.54(5)
0.4	0.0053	7.885(18)	179.70(18)
0.5	0.0053	7.779(12)	179.28(9)

Table 4
Selected interatomic distances (Å) in $YBa_2(Fe_{1-z}Co_z)_3O_{8+w}$ at 295 K

Bond	$z = 0.0$	$z = 0.2$	$z = 0.3$	$z = 0.4$	$z = 0.5$
Fe/Co(1)–O(1)	2.1543(36)	2.1505(36)	2.1419(36)	2.1497(36)	2.1418(36)
Fe/Co(1)–O(3)	1.9576(1)	1.9561(1)	1.9544(1)	1.9531(1)	1.9525(1)
Fe/Co(2)–O(1)	1.8566(60)	1.8480(59)	1.8503(59)	1.8249(59)	1.8313(59)
Fe/Co(2)–O(2)	2.0206(12)	2.0173(12)	2.0149(12)	2.0165(12)	2.0147(12)
Fe/Co(2)–O(2′)	1.9576(1)	1.9561(1)	1.9544(1)	1.9531(1)	1.9525(1)
Fe/Co(2)–O(4)	1.8944(24)	1.8868(24)	1.8856(24)	1.8894(24)	1.8852(24)
Ba–O(1)	2.7751(6)	2.7726(5)	2.7688(5)	2.7697(6)	2.7660(5)
Ba–O(2)	3.2138(48)	3.1957(48)	3.1782(47)	3.1987(47)	3.1659(47)
Ba–O(2′)	2.8331(35)	2.8219(35)	2.8078(35)	2.8179(35)	2.7917(34)
Ba–O(3)	2.7722(26)	2.7723(26)	2.7793(26)	2.7552(26)	2.7792(26)
Y–O(2)	2.4030(14)	2.4018(33)	2.4014(14)	2.3957(14)	2.3958(14)
Y–O(2′)	2.7242(9)	2.7178(9)	2.7157(9)	2.7174(9)	2.7141(9)
Y–O(4)	2.7685(1)	2.7663(1)	2.7639(1)	2.7620(1)	2.7612(1)
O(2)–O(1)	2.6980(33)	2.6910(33)	2.6913(33)	2.6729(33)	2.6769(33)
O(2′)–O(4)	2.7242(9)	2.7178(9)	2.7157(9)	2.7174(9)	2.7141(9)

Table 5
Bond-valence sums from refined atomic coordinates of $YBa_2(Fe_{1-z}Co_z)_3O_{8+w}$

Atom	$z = 0.0$ $w = 0.068$	$z = 0.2$ $w = 0.034$	$z = 0.3$ $w = 0.033$	$z = 0.4$ $w = 0.026$	$z = 0.5$ $w = 0.047$
Fe/Co(1)	3.02(4)	2.93(4)	2.91(4)	2.85(3)	2.83(3)
Fe/Co(2)	2.76(6)	2.67(6)	2.64(6)	2.64(5)	2.62(5)
Fe/Co average	2.85(5)	2.76(5)	2.73(5)	2.71(5)	2.69(5)
Ba	2.50(4)	2.50(4)	2.51(4)	2.56(4)	2.54(4)
Y	2.76(5)	2.81(6)	2.81(6)	2.86(5)	2.84(5)
O(1)	2.16(4)	2.15(4)	2.15(4)	2.18(4)	2.16(4)
O(2)	1.84(4)	1.83(4)	1.83(4)	1.81(3)	1.82(3)
O(2′)	1.90(3)	1.89(3)	1.90(4)	1.87(3)	1.89(3)
O(3)	2.24(3)	2.20(3)	2.17(3)	2.22(3)	2.14(3)
O(4)	1.89(17)	1.88(30)	1.86(37)	1.84(31)	1.83(18)

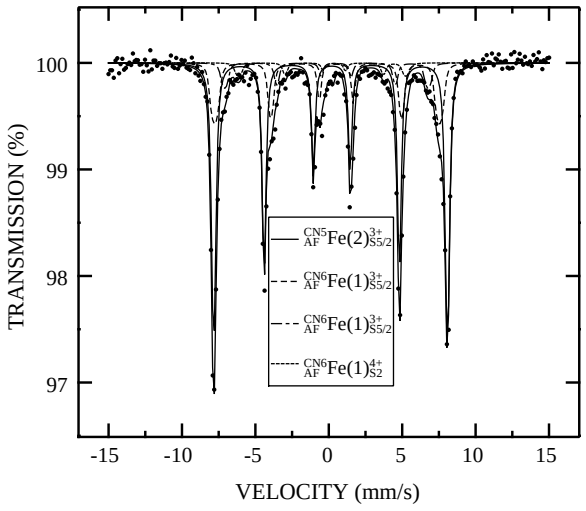

Fig. 2. The fitted (295 K) ^{57}Fe spectrum for $YBa_2(Fe_{0.7}Co_{0.3})_3O_{8.033}$. The component labels are shown in the legend.

why w increases somewhat towards the Co substitution limit, and, in general, why Co maintains such a relatively high valence.

3.3. Mössbauer spectroscopy

The typical ^{57}Fe Mössbauer spectrum of $YBa_2(Fe_{1-z}Co_z)_3O_{8+w}$ shown in Fig. 2 is composed of four components corresponding to various iron valence- and spin-states. Two components are strong and are identified according to their hyperfine parameters as the AF-ordered, HS trivalent iron located at the six- and five-coordinated sites Fe(1) and Fe(2), respectively, $^{CN6}_{AF}Fe(1)^{3+}_{S5/2}$ and $^{CN5}_{AF}Fe(2)^{3+}_{S5/2}$ in shorthand. The square-pyramidally coordinated iron, $^{CN5}_{AF}Fe(2)^{3+}_{S5/2}$, maintains its relative Mössbauer intensity constant across the substitution range of Co, and this once again confirms that both iron coordinations (sites) accommodate the same relative amount of Co. The octahedral $^{CN6}_{AF}Fe(1)^{3+}_{S5/2}$ component decreases in intensity with

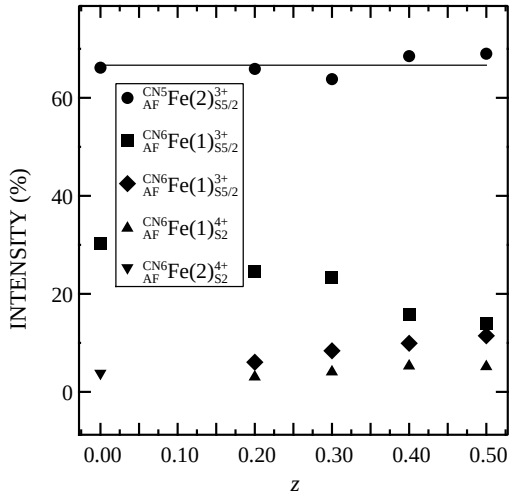

Fig. 3. Relative component intensities in Mössbauer spectra of $YBa_2(Fe_{1-z}Co_z)_3O_{8+w}$ at 295 K. The theoretical 66.7% portion of Fe(2) is indicated.

increasing z in $YBa_2(Fe_{1-z}Co_z)_3O_{8+w}$, but this is compensated by the increasing intensity of the two weaker components (Fig. 3) which hence also must be located at the Fe(1) site. The negative isomer shift (Fig. 4) and the somewhat weaker magnetic field (Fig. 5) clearly suggest the assignment of an HS state $^{CN6}_{AF}Fe^{4+}_{S2}$ to the weaker of the two minority components, whereas the isomer shift of the stronger minority component is typical of trivalent iron. Therefore, we must conclude that the latter is a companion to the main trivalent component at Fe(1) which differs only in the value of B. Note that none of these components originates from the secondary phase $(Ba,Y)(Co,Fe,Y)O_{\sim 3}$, which is paramagnetic at 295 K and present in much smaller concentrations. Showing only a small quadrupole splitting, the Mössbauer spectrum of this cubic phase coincides with that of the iron impurity in the Be and Al parts of the instrument. The Mössbauer characteristics have been verified on a pure $Ba(Fe,Y)O_{\sim 3}$ sample originating from Ref. [7].

As mentioned, both minority components increase in intensity with the increasing Co substitution level z. The increase in the intensity of the tetravalent component corresponds to the Co oxidation state being kept near 3.00, since the PND-determined amount w of the excess oxygens remains approximately constant while the iron content decreases. The emerging Fe^{4+} ions are of the Fe(1) type, and the balance thus implies that the cobalt substituent at the Fe/Co(2) site occupies primarily locations hosting the excess oxygens O(4) in their coordination sphere. This is the only manifestation of the excess oxygens in the Mössbauer spectra for $z > 0$. These findings make sense because Co^{3+} has a smaller single-bond radius than Fe^{3+}, and hence requires more bonding when the structural framework is rigid. The

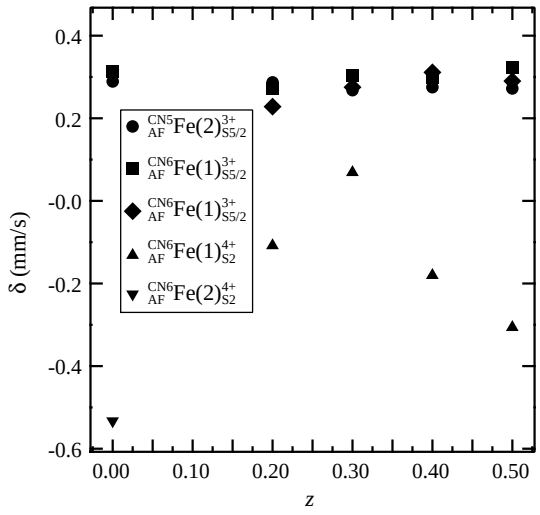

Fig. 4. Isomer shifts for the Mössbauer components of $YBa_2(Fe_{1-z}Co_z)_3O_{8+w}$ at 295 K.

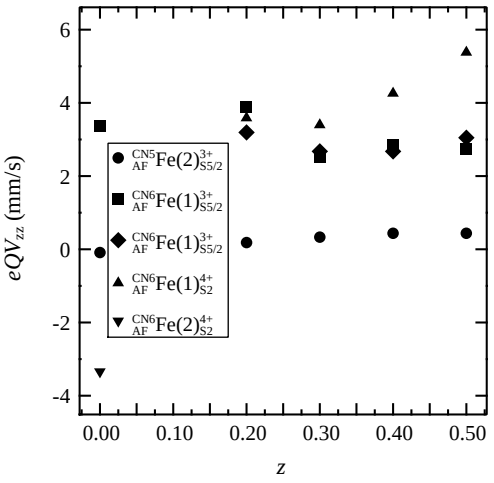

Fig. 6. Quadrupole coupling constants for the Mössbauer components of $YBa_2(Fe_{1-z}Co_z)_3O_{8+w}$ at 295 K.

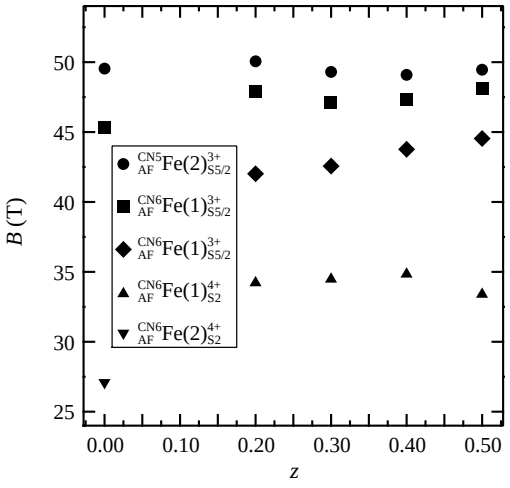

Fig. 5. Internal magnetic fields for the Mössbauer components of $YBa_2(Fe_{1-z}Co_z)_3O_{8+w}$ at 295 K.

sixth oxygen around Fe/Co(2) brings about some 0.5 valence units, and this is more than enough to compensate the valence deficit caused by the difference between the iron and cobalt single-bond radii. The excess charge at the locally formed Co(2) octahedral site is then transferred by bond relaxation to the adjacent Fe(1) octahedron where Fe^{4+} emerges. In the pure solvent phase, however, ($YBa_2Fe_3O_{8.07}$ in this case), the tetravalent iron resides at the Fe(2) site, occupying those positions where the added oxygen ($w = 0.07$) created an octahedral environment [17].

The increase in the $^{CN6}_{AF}Fe(1)^{3+}_{S5/2}$ companion component suggests at first that it has its origin in structural distortions or disturbances of the magnetic order owing to Co. However, such interpretation is interesting to confront with the fact that this component is absent in the 77 K spectra (which otherwise have the same features as the corresponding room-temperature spectra). At present there is no clearcut explanation, but a possibility is that the companion is involved in an oscillating mixed-valence state which undergoes charge localization at low temperatures [20].

Once the assignments are established, the Mössbauer parameter which tells most about the local structural environments is the quadrupole coupling constant (Fig. 6). The Fe(2)-site component, $^{CN5}_{AF}Fe(2)^{3+}_{S5/2}$, has eQV_{zz} close to zero and this is as expected for a square pyramidal coordination having the central iron atom close to the center of gravity [17]. On the other hand, eQV_{zz} is large and positive for all the three Fe(1)-site components, and this means that the octahedron must be elongated along the c-axis (a compression would have given a negative eQV_{zz}). Furthermore, the angle θ between the directions of the electric field gradient V_{zz} and the internal field B gives consistently the best fit when set equal to 90° for all three components for the octahedral site. According to PND (Section 3.2), the internal field vector is located in the a, b plane, and this means that V_{zz} must be parallel with the c-axis. No oxygen is hence missing along the a or b axes in the Fe(1) neighborhood, otherwise the thus obtained CN5 environment would have the direction of V_{zz} perpendicular to the c-axis (assuming point-like charges and no major lattice distortions) even though V_{zz} could remain positive.

4. Concluding remarks

The Co substitution in the triple-perovskite-type structure of $YBa_2Fe_3O_{8+w}$ illustrates how small

differences in atomic size (probed as single-bond size) can affect the stability of structures with fixed coordination geometries. The Co atom is perfectly suited for both octahedral and square-pyramidal environment, and indeed random distribution is achieved over the iron sites in the $YBa_2Fe_3O_8$ structure. Both T ions are trivalent, in their HS states, and the AF arrangement of the parent structure is maintained throughout the solid-solution range. Mössbauer spectroscopy shows that an increasing amount of tetravalent Fe in an internal redox equilibrium helps to keep the Co valence near 3.00 under increasing Co substitution, while a diminishing amount of Fe ions experiences the extra charge of the added oxygens w. The observed stability limit at $z = 0.47(5)$ appears to arise from the fact that the single-bond radius of Co^{3+} is smaller than that of Fe^{3+}. The resulting tendency to contract both the coordination square pyramid and the octahedron is poorly accepted by the barium atom which already in the parent structure is overbonded. A different situation can be drawn for $YBa_2Cu_3O_7$. Here the CN4 for Cu, instead of CN6 for Fe, permits longer bonds, and, in fact, the single-bond length of Co^{2+}–O is slightly longer than that of Cu^{2+}–O. Hence, cobalt can substitute for Fe and Cu in both structures, but the important distinction is that it is Co^{3+} that constitutes the substituent in $YBa_2Fe_3O_8$ (as identified in this study) whereas Co^{2+} is the predominant substituent in $YBa_2Cu_3O_7$ [6]. An extension of these arguments explains why very little substitution of copper occurs for iron in $YBa_2Fe_3O_8$ [4].

References

[1] R.J. Cava, A.W. Hewat, E.A. Hewat, B. Batlogg, M. Marezio, K.M. Rabe, J.J. Krajewski, W.F. Peck, L.W. Rupp, Physica C (Amsterdam) 165 (1990) 419.
[2] P. Karen, H. Fjellvåg, A. Kjekshus, J. Solid State Chem. 97 (1992) 257.
[3] Q. Huang, P. Karen, V.L. Karen, A. Kjekshus, J.W. Lynn, A.D. Mighell, N. Rosov, A. Santoro, Phys. Rev. B 45 (1992) 9611.
[4] P. Karen, P.H. Andersen, A. Kjekshus, J. Solid State Chem. 101 (1992) 48.
[5] P. Karen, A. Kjekshus, J. Solid State Chem. 112 (1994) 73.
[6] P.H. Andresen, H. Fjellvåg, P. Karen, A. Kjekshus, Acta Chem. Scand. 45 (1991) 698.
[7] P. Karen, P.H. Andresen, A. Kjekshus, J. Solid State Chem. 101 (1992) 48.
[8] P. Karen, A. Kjekshus, J. Am. Ceram. Soc. 77 (1994) 547.
[9] P.E. Werner, The Computer Programme SCANPI9, Institute of Inorganic Chemistry, University of Stockholm, Sweden, 1992.
[10] J. Fiala, Silikaty 29 (1985) 273.
[11] H.M. Rietveld, J. Appl. Crystallogr. 2 (1969) 65.
[12] A.C. Larson, R.B. Von Dreele, General structure analysis system, Los Alamos National Laboratory Report LAUR 86-748, 1994.
[13] J. Lindén, M. Lippmaa, P. Karen, A. Kjekshus, M. Karppinen, J. Solid State Chem. 138 (1998) 87.
[14] I. Felner, I. Nowik, U. Yaron, O. Cohen, E.R. Bauminger, T. Kroener, G. Czjzek, Phys. Rev. B 48 (1993) 16 040.
[15] A.J. Jacobson, J.L. Hutchison, J. Solid State Chem. 35 (1980) 334.
[16] T. Negas, R.S. Roth, NBS Spec. Publ. (U.S.) 364 (1972) 233.
[17] J. Lindén, A. Kjekshus, P. Karen, J. Miettinen, M. Karppinen, J. Solid State Chem. 139 (1998) 168.
[18] I.N. Sora, Q. Huang, J.W. Lynn, N. Rosov, P. Karen, A. Kjekshus, V.L. Karen, A.D. Mighell, A. Santoro, Phys. Rev. B 49 (1994) 3465.
[19] I.D. Brown, Accumulated table of bond valence parameters, version 1999.03.26, personal communication.
[20] J. Lindén, P. Karen, A. Kjekshus, J. Miettinen, T. Pietari, M. Karppinen, Phys. Rev. B 60 (1999) 15251.